Bulletin of Atmospheric Science and Technology (2025) 6:24
https://doi.org/10.1007/s42865-025-00110-4

CASE STUDY

Using ground-based lidar data to investigate the water–vapor budget in the daytime atmospheric boundary layer

Diego Lange[1] · Andreas Behrendt[1] · Christoph Senff[2,3] · Timothy J. Wagner[4] · Florian Späth[1] · Volker Wulfmeyer[1]

Received: 31 December 2024 / Revised: 30 June 2025 / Accepted: 8 July 2025

Abstract
The moisture advection term in the water–vapor budget equation is investigated with a combination of a vertically-staring water–vapor lidar and Doppler lidar systems. These instruments make it possible to get the mean profile of moisture tendency and the latent heat flux (LHF) divergence. We use data of the Land–Atmosphere Feedback Experiment (LAFE) at the Atmospheric Radiation Measurement (ARM) Program's Southern Great Plains (SGP) site, Oklahoma, USA, collected on 30 August 2017 between 15 and 24 UTC, which corresponds to 09 to 18 LT. The lidars provide turbulence resolving profiles of moisture and vertical wind fluctuations. The LHF profile is derived from the covariance of these moisture and vertical wind fluctuations. The mean boundary layer height z_i is determined from the peak of the moisture variance. The results demonstrate that the combination of two remote sensing instruments can be applied for determining the dominant water–vapor budget terms, namely moisture tendency, latent heat flux divergence and moisture advection.

Keywords LidarWater vapor budgetAtmospheric boundary layerAdvectionTurbulence

1 Introduction

The land–atmosphere (LA) system consists of soil and land cover including e.g., vegetation, and the overlying atmosphere. The convective boundary layer (CBL) plays a key role in the exchange of moisture, heat, and momentum inside the LA system, in response to the heat

✉ Diego Lange
diego.lange@uni-hohenheim.de

[1] Institute of Physics and Meteorology, University of Hohenheim, Stuttgart, Germany

[2] NOAA Chemical Sciences Laboratory, Boulder, CO, USA

[3] Cooperative Institute for Research in the Environmental Sciences, University of Colorado, Boulder, CO, USA

[4] Space Science and Engineering Center, University of Wisconsin–Madison, Madison, WI, USA

introduced by the sun. Over the diurnal cycle, the water–vapor and energy budgets control the evolution of temperature, humidity, and momentum in the CBL, which are related to convection initiation, the formation of shallow and deep clouds, and thus precipitation. Therefore, the understanding of the CBL evolution and its structure is fundamental for accurate weather and climate simulations (Behrendt et al. 2011; Santanello et al. 2011; Wulfmeyer et al. 2015).

The LHF and its divergence (LFD) is a key component of the moisture budget in the CBL, which is influenced by atmospheric dynamics inside the CBL and moisture advection (MAD); however, this is a strongly under-observed quantity.

Improving our understanding of the LA system requires simultaneous measurements in all compartments of the system. In particular, observations of the surface energy balance closure are necessary. These data sets are traditionally available from field studies and monitoring networks using radiation, ground heat flux, and eddy covariance measurements. However, LA feedback studies using measurements constrained to the land surface are strongly limited because of the feedbacks with CBL dynamics, thermodynamics and fluxes (Wulfmeyer et al. 2015).

To observe the water–vapor budget in the CBL, a variety of measurements can be used. In the past, CBL and entrainment fluxes have been mainly determined by aircraft and balloons (Lenschow et al. 1994), a relatively sparse and expensive method. Other methods include ground-based and satellite-based remote sensing instruments, such as water–vapor Raman lidars, or microwave radiometers. These measurements can provide information on the spatial and temporal variability of water vapor in the atmosphere and can be used to investigate the processes that control the water–vapor budget. However, the lack of high-resolution temperature and water–vapor profiles, their gradients, and their turbulent fluctuations was a major weakness for monitoring the CBL diurnal cycle and feedback processes (Wulfmeyer et al. 2015). Another approach to estimate MAD at SGP has been made by Wagner et al. (2022), using a instrument synergy on a different date (8 August 2017) and an output from the High-Resolution Rapid Refresh numerical weather prediction model. Furthermore, large eddy simulations (LES) have also been used for simulate the evolution of the CBL during LAFE (Bauer et al. 2023), and also to specifically compare and evaluate the evolution of the water vapor-budget in the CBL (Wakefield et al. 2023).

A new approach for turbulence profiling involves the use of ground-based lidar systems, including Doppler lidar (DL) for wind measurements, temperature rotational Raman lidar (TRRL, Hammann et al. 2015; Lange et al. 2019; Radlach et al. 2008), and either WVDIAL (Wagner et al. 2013) or a water–vapor Raman lidars (WVRL, Lange et al. 2019; Whiteman 2003a, 2003b). DL instruments can be employed to investigate higher-order turbulent moments of vertical wind and estimate the turbulent kinetic energy dissipation rate (Lenschow et al. 2012). WVDIAL and WVRL resolve turbulent moments of water–vapor fluctuations up to the fourth order up to the CBL top and into the entrainment layer (Weckwerth et al. 1999; Wulfmeyer et al. 2010; Turner et al. 2014; Muppa et al. 2016; Di Girolamo et al. 2017). One example includes the use of TRRL for profiling turbulent temperature fluctuations, combined with DL to measure sensible heat fluxes (Behrendt et al. 2020).

In this regard, the Land–Atmosphere Feedback Experiment was performed in August 2017 at the ARM Program's SGP site (Sisterson et al. 2016) in Oklahoma USA (36.607 N, 97.488 W, 314 msl). Throughout this campaign, an innovative combination of scanning lidar systems alongside various in-situ and remote sensing instruments delivered precise 3D measurements of multiple dynamical and thermodynamical variables, enhancing our ability to assess and deepen understanding of LA interactions (Wulfmeyer et al. 2018). One of the LAFE scientific objectives was to characterize LA feedback and the moisture budget at the SGP site, which is addressed in this paper, taking advantage of the novel synergy provided by Raman and Doppler lidars at the site to compute the water–vapor budget variables.

This paper is divided into several sections. After this introduction, Sect. 2 describes the instruments used in this study. Section 3 explains the methodology employed to obtain the needed variables for the calculation of the water–vapor budget. In Sect. 4, a case study is presented, and finally, a summary and conclusions are given in Sect. 5.

2 Instrumental setup

The sensor synergy employed during LAFE involved a large setup of instruments. In this study, we use data of the SGP Raman lidar (SRL), SGP Doppler lidar (SDL) pointing vertically, and the University of Hohenheim Doppler lidar (UHDL) performing velocity azimuth display (VAD) scans. This combination permits the profiling of temperature, humidity, and horizontal and vertical wind as well as turbulent variables such as higher-order moments and LHF (Wulfmeyer et al. 2018). Their location can be seen in Wulfmeyer et al. (2018).

2.1 SGP water–vapor Raman lidar

The SRL is an automated system primarily developed for measuring atmospheric water vapor profiles (Goldsmith et al. 1998; Turner and Goldsmith 1999). It emits 355-nm radiation pulses into the atmosphere at 30 Hz with a pulse energy of ~300 mJ. The lidar detects backscattered signals in channels tuned to elastic scattering, as well as vibrational Raman scattering from water vapor and nitrogen. Its telescope has a diameter of 61 cm, and two fields of view for signals close to the surface (low channels) and higher in the atmosphere (high channels). Data are processed using automated routines (Thorsen & Fu 2015; Turner et al. 2002). All the data are provided through the ARM Data Archive (https://adc.arm.gov/discovery/). The native SRL resolution is 10 s and 7.5 m. For our study, we use the water–vapor mixing ratio (WVMR) measured by the SRL.

2.2 Doppler wind lidars

Data from two DLs deployed at the SGP site during LAFE were used to obtain the vertical and horizontal wind. Both vertically pointing and VAD scanning DLs are commercially available at Halo Photonics Streamline systems (Pearson et al. 2009). This lidar type uses a heterodyne approach to determine the Doppler velocity along the line of sight, with 1.5 µm laser pulses at 10 kHz. Backscattered raw data have 1 s and 30 m resolution.

The SDL, observed the vertical wind in a constant vertical staring mode. The UHDL was operated in six-beam VAD mode during LAFE, to measure profiles of horizontal wind (Choukulkar et al. 2017). Following Bonin et al. (2017), one beam is vertical, and the other five set to elevation angle of 45°, equally spaced 72° apart in azimuth. A complete scan takes approximately 27 s.

3 Methodology

VAD measurements also provide turbulence-resolving capabilities, enabling the estimation of turbulent kinetic energy (TKE) and momentum fluxes. Wulfmeyer et al. (2016) demonstrated that a synergy between Raman lidars and DL can be used to determine

fluxes throughout the CBL and for developing new turbulence parameterizations. When combined with additional cross-track scanning DLs, this configuration supports surface-layer profiling (Späth et al. 2016, 2022) and facilitates the mapping of land surface fluxes.

3.1 Latent heat flux analysis

Lenschow et al. (2000) introduced a method for estimating higher-order moments of turbulent fluctuations that accounts for random instrumental noise. This approach is able to distinct the higher-order moments of temperature, vertical wind, and humidity from the moments caused by instrument noise uncertainties. Wulfmeyer et al. (2016) refined this technique by incorporating features like automated spike detection and optimized lag selection for autocovariance analyses. CBL flux profiles have been derived using the eddy covariance method (Senff et al. 1994; Wulfmeyer 1999). Detailed descriptions of the data processing procedure are provided in detail in Behrendt et al. (2020) and Wulfmeyer et al. (2016).

First, WVMR (m) from the SRL and vertical wind (w) from the SDL were despiked, This involved computing histograms of the data at each height over the selected time period, and removing data outside of four standard deviations from the median. This step is essential because lidar processing algorithms are non-linear, and noise can produce large outliers in some cases (Behrendt et al. 2020).

Next, the despiked m data were detrended using a linear fit at each height level. Then, the detrended m and despiked w data were high-pass filtered with a cutoff of 30 min. This is necessary in order to concentrate on the turbulent fluctuations by removing influences of the diurnal cycle, large-scale advection and synoptic processes.

Both procedures must be performed with caution, so real atmospheric features are not eliminated. An averaging time of one hour is typically long enough to include enough large turbulent eddies to reduce the flux sampling errors to acceptable levels (calculated every 10 min). For this time period the turbulence was considered to be quasi-stationary, so that the ensemble mean of a turbulent variable could be replaced by the time average at a fixed point in space (Lenschow et al. 1994). Also, it is important that the time and height for each data point are as close as possible, before m and w time series can be combined. Therefore, the data is gridded to the closest neighbours. The native SRL resolution is 10 s and 7.5 m and the native DL resolution is one second and 30 m. In this study, both SRL and SDL data was gridded to 10 s and 50 m (Behrendt et al. 2020). This procedure generated profiles of the time series of the WVMR and vertical wind fluctuations $m\prime(t, z)$ and $w\prime(t, z)$ respectively, where z is the height above ground level.

The covariance between $m\prime$ and $w\prime$ provides profiles of the eddy LHF according to

$$LHF(z) = \overline{m'w'(z)} \tag{1}$$

The vertical LFD can be calculated after

$$LFD(z) = \frac{\partial\left(\overline{m'w'(z)}\right)}{\partial z} \tag{2}$$

And the WVMR tendency (WVT)

$$WVT = \frac{\partial \overline{m}}{\partial t} \tag{3}$$

It is important to note that for the calculation of LFD(z), only the lidar data was used, no surface data of the LHF are needed.

3.2 Water–vapor budget

Following Wulfmeyer (1999), LFD and WVT can be applied to estimate MAD, through the water–vapor budget equation according to

$$MAD \approx -LFD - WVT \tag{4}$$

where MAD is generally the combination of horizontal and vertical advection. The vertical advection $w\frac{\partial m}{\partial z}$ may be estimated, if the subsidence is known, but this is usually both difficult with respect to measurements and modelling. Furthermore, we neglected horizontal divergence of latent heat flux as well as source and diffusion terms, because they are comparatively small in the SGP site, similar to previous studies like Wulfmeyer (1999).

4 Case study

A daytime period was selected where the evolution of the CBL is observable, where few boundary layer clouds were present, and during which all the necessary instruments were measuring. The chosen period is August 30, 2017 from 15 to 24 UTC (10 to 19 LT). The maximum elevation of the sun corresponds to 18:30 UTC (13:30 LT). Sunrise and sunset were at 11:59 UTC and at 01:00 UTC respectively. The deployment locations of the lidars and flux towers are shown in Fig. 4 of Wulfmeyer et al. (2018).

We start with the measurements needed for the budget calculation, that are, WVMR from the SRL and vertical wind from the SDL. Next, the LHF, WVMR tendency and flux divergence are computed. With these parameters, we determine the moisture advection, as explained in the previous section.

The LHF shows the daily cycle of latent heat transfer at the Earth's surface through evaporation and transpiration. In this case study, measurements from three of the eddy covariance (EC) towers closest to the SGP lidar position were considered (Fig. 1). EC1 and EC3 were located in farm fields, and EC2 was located in a native grass field. We use a Gaussian fit as an approximation to the evolution of the surface fluxes.

It can be observed that while the shape of the measurements corresponds to a diurnal cycle, the magnitudes are different. At 17 UTC for example, tower one measured 140 W m^{-2}, while tower two measured 210 W m^{-2}, and tower three 195 W m^{-2}. This difference can be explained by the different types of crops where the towers were located. Sharp changes can be explained by the appearance of clouds, for example. During LAFE, most of the measurement days were cloudy. This case study is one of the least cloudy days.

As explained in the previous section, to close the water–vapor budget, it is necessary to know the WVMR tendency, LHF and its divergence. Consequently, the WVMR and vertical wind speed measured by the lidars are needed, so that the fluctuations in each variable can be obtained and used for the LHF calculation.

To address the representativeness of the calculated advection, and whether the assumptions made in the previous section are valid, horizontal wind speed and direction are shown in Fig. 2.

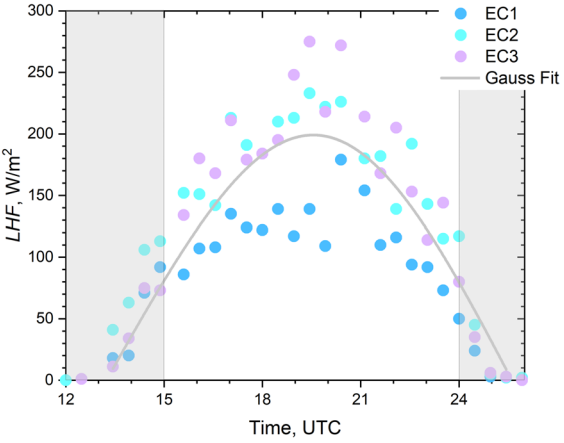

Fig. 1 Surface energy flux measurements from three 10 m EC towers between 30 August 2017 at 12:00 UTC and 31 August 2017 at 02:00 UTC (coloured dots). Local noon was at 18:30 UTC (13:30 LT). EC1 and EC3 were located in farm fields, and EC2 was located in a native grass field. A Gaussian fit (gray line) shows the overall temporal evolution. The maxima LHF measured at the surface is found at about 19:30 UTC which is about 1 h after local noon at 18:30 UTC

Horizontal wind direction is fairly constant during the whole measurement period, from a NE direction between 40 and 60 degrees. The horizontal wind speed remains relatively constant within the CBL, around 6 to 7 m s^{-1}.

As explained in the previous section, data was averaged over one hour every 10 min. If the wind speed is about six meters per second, the distance travelled by the advected moisture is about 22 km. The validity of this assumption needs to be confirmed using numerical models or other remote-sensing data.

Figure 3 shows the WVMR and its variance. In both plots, the evolution of the CBL can be clearly observed. z_i is determined from the peak of the WVMR variance. The height of the CBL top (z_i, Fig. 4) can be influenced by factors like surface heating, atmospheric stability, and advection of air masses and was estimated looking for the peak in the atmospheric WVMR variance (following Turner et al. 2014).

It has been previously mentioned that this day was one of the least cloudy. In Fig. 3a, the cloud base is marked with black dots. There were only a few small clouds. Figure 3c

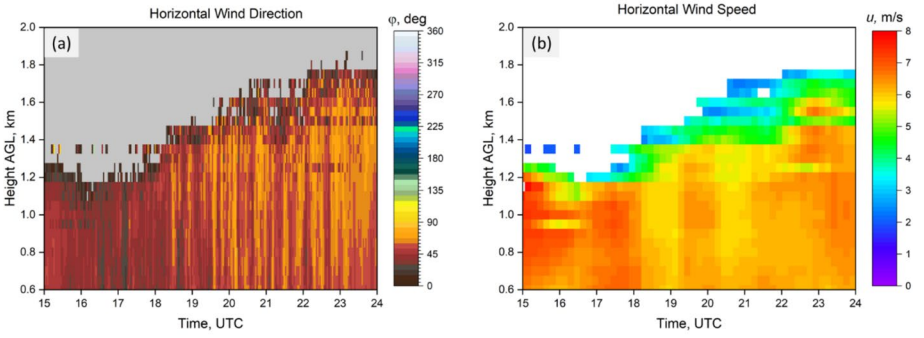

Fig. 2 Time-height cross sections of (**a**) horizontal wind direction, and (**b**) horizontal wind speed measured on 30 August 2017 between 15 and 24 UTC with the scanning Doppler lidar (UHDL). The data show that horizontal wind speed and direction are fairly constant in this case. The temporal and spatial resolutions are (a) 120 s and 50 m and (b) are 600 s and 50 m

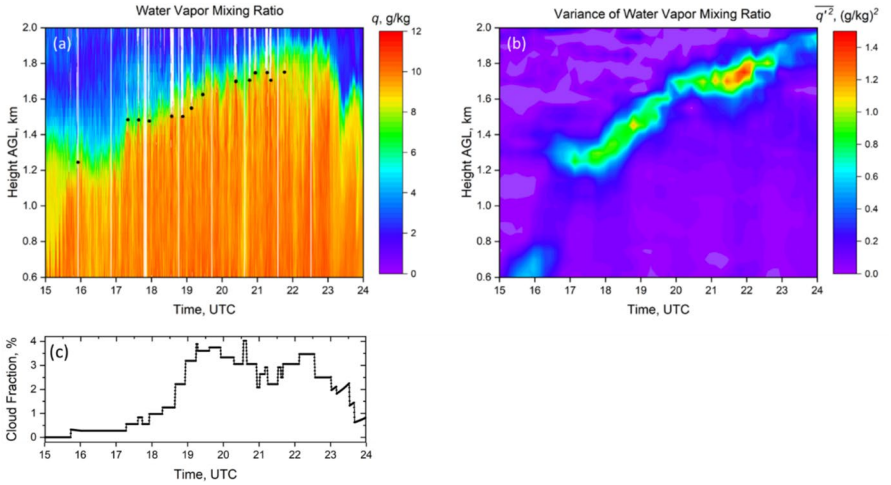

Fig. 3 Time-height cross sections of (**a**) WVMR and (**b**) the variance of turbulent WVMR fluctuations measured with the vertically-pointing water–vapor Raman lidar (SRL). Same height and time period as in Fig. 2. The temporal and spatial resolutions are (a) 10 s and 50 m, and (b) 10 min and 50 m (gliding one-hour-average every 10 min). (**c**) Cloud fraction (gliding one-hour average)

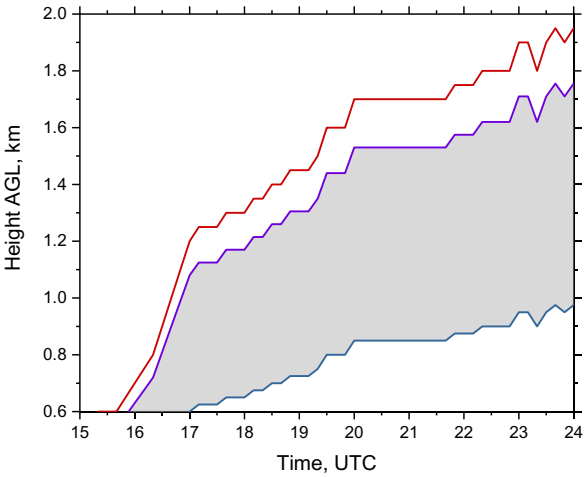

Fig. 4 CBL top height z_i (red) determined with the peak of the atmospheric WVMR variance (Fig. 3b). The gray area shows the CBL between 0.5 z_i and 0.9 z_i. This region is used for the data averages of the water–vapor budget terms

shows that cloud fraction on this day is small with maximum of 4%. Therefore, we consider the influence of these clouds is small.

Advection throughout the day can affect the height of the top of the CBL by transporting air masses with different temperature, humidity, and momentum properties. The vertical wind speed variance also indicates that the air masses inside the CBL are mixing, and turbulence is present, which supports the assumption of a so-called CBL (Fig. 5b).

It is important to know the evolution of z_i, to be able to determine where turbulence processes are present inside the CBL, in order to close the water–vapor budget. In Fig. 4, it is shown as a function of the time of day. We decided to use data between 0.5 z_i and 0.9 z_i, so

that the moisture advection calculation is representative for that region (Fig. 4). Above 0.9 z_i, the interfacial layer begins. We chose 0.5 z_i, because at that height the CBL is representative of a well-mixed layer. The vertical wind variance (Fig. 5b) also shows that turbulence is taken place in that region.

Once moisture and vertical wind data are available from the lidar systems, the WVMR tendency, LHD and MAD can be estimated (Fig. 6).

Flux divergence, shown in Fig. 6b, changes throughout the day because it is affected by a variety of factors, including changes in atmospheric circulation patterns, variations in surface heating and cooling, humidity levels in the lower free troposphere above the CBL top, and the movement of air masses. Therefore, changes in flux divergence during the day can reflect changes in atmospheric dynamics and surface conditions, observed in Fig. 3 and Fig. 5. The LHF profiles are influences by both sampling statistics of the turbulent transport during our observation time period (which is, one hour) and system noise. We like to stress that even though the structures noted in LHD are a result of the turbulent structure and sampling in the atmosphere during the day, noise in the measurements propagates when calculating LHF and LHD. See also the uncertainties shown in Fig. 8 and Fig. 9 (obtained from the lidar data). The WVMR tendency shows a peak at the top of the CBL (Fig. 6c), while inside the CBL it is fairly constant. Because of the increase of z_i over the course of the day, the beginning of a one-hour times series at an altitude near the top of the CBL tends to lie in the drier lower free troposphere, while the latter part of the time series lies within the moister CBL, resulting in a positive WVT (e.g., Figs. 3a and 6c, 1.3 km, 18:15 UTC). The high WVT values in Fig. 6c follow z_i.

As a result, moisture advection shown in Fig. 6d, reflects mainly the changes in the flux divergence inside the CBL, given that WVMR tendency does not fluctuate as much as the divergence.

Figure 7 shows the area-averaged MAD obtained with the approach of Wagner et al (2022). In this alternate method originally proposed by (Michael, (1994), a network of Doppler lidars identical to the SDL are collocated with ground-based infrared radiometers at four sites surrounding the SGP central facility (Four nodes from the ARM SGP profiling network, with distances between each other of 50 to 80 km apart). Profiles of temperature and water vapor are obtained from the infrared observations using the Tropospheric Remotely Observed Profiling via Optimal Estimation (TROPoe, Turner and

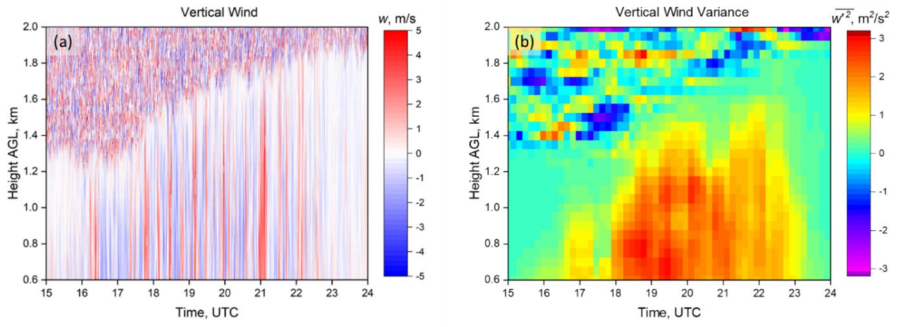

Fig. 5 Time-height cross sections of (**a**) vertical wind and (**b**) vertical wind variance measured with the vertically-pointing Doppler lidar (SDL). Same height and time period as in Fig. 2. The temporal and spatial resolutions are (a) 10 s and 50 m, and (b) 600 s and 50 m (gliding one-hour-average every 10 min)

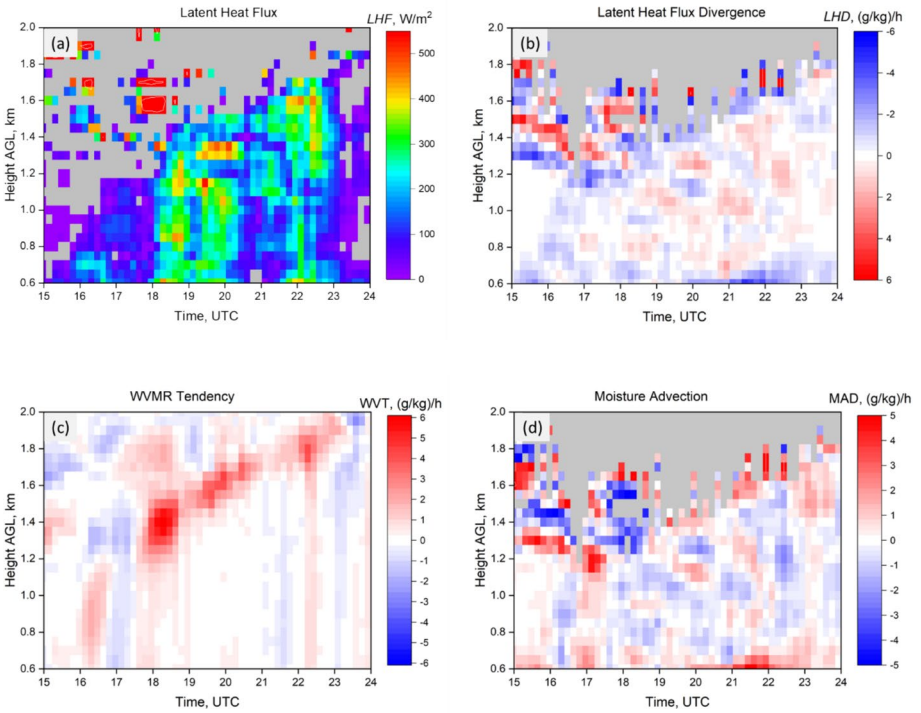

Fig. 6 Time-height cross sections of (**a**) LHF, (**b**) LFD, (**c**) WVT, and (**d**) MAD calculated with the vertically-pointing water–vapor Raman lidar (SRL) and the vertically-pointing Doppler lidar (SDL) data. The height and time period are the same as in Fig. 2. The temporal and spatial resolutions are 10 min and 50 m respectively (gliding one-hour-average every 10 min)

LöHnert 2014; Turner and Blumberg 2019; Turner and LöHnert 2021) algorithm. The circulation around the polygon defined by the observing sites can easily be estimated using the observations, and Green's Theorem can be applied to relate that circulation to

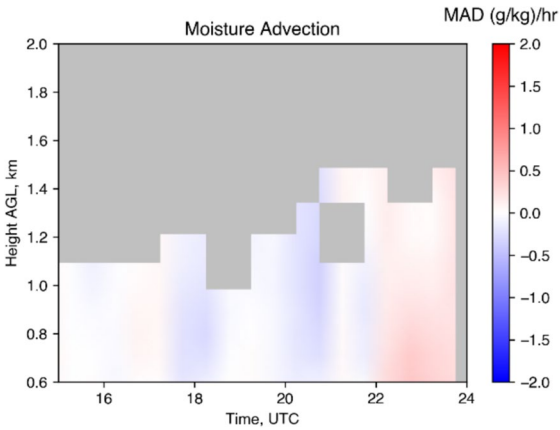

Fig. 7 Time-height cross sections of area-averaged MAD calculated using Wagner et al. 2022 technique (30 min), over a larger domain

the areal-averaged advection within that domain. Despite differing temporal resolutions (hence the reduced variability in Fig. 7), similar trends can be observed above 0.6 km, although the values are higher in Fig. 6d. Due to the nature of passively-observed thermodynamic profiling, the vertical spacing of the observation grid is not constant, but increases with increasing height.

A comparison between the LHF between 0.5 z_i and 0.9 z_i is shown in Fig. 8 together with its uncertainty, and the averaged surface flux from the three EC towers shown in Fig. 1. Although the evolution of the surface fluxes is somehow different from that calculated using the lidar data, both datasets are in almost all cases within the expected uncertainty for the lidar measurements, except for those measurements towards the end of the day. In this period, between 2200 to 2330 UTC, the LHF values calculated using the lidars are smaller than the EC data, showing that the LHF at the surface is larger than in the upper CBL in this period of the day. The two datasets cover different parts of the CBL. A good agreement of LHF between surface and upper CBL means that LFD across the CBL is small.

In Fig. 9, MAD, WVT, and LFD evolution and their error bars are shown in two different ways. Figure 9a shows their averaged values over the selected time period. WVT is positive until 20:30 UTC, when it becomes negative until the end of the day, representing an afternoon drying trend, while the LFD tends to increase over the same period. MAD responds to changes in both LFD and WVT. In the following, we discuss some of the details shown in Fig. 9a.

It is interesting to note that the positive and negative values of MAD seem to correlate often with the independent data of the horizontal wind (Fig. 2). While, e.g., the larger wind velocity values between 17 and 18 UTC from northern direction correlate with comparatively larger positive MAD $> 1.21 \pm 0.07$ (g kg^{-1}) h^{-1}, the smaller easterly horizontal wind values later between about 19 and 21 UTC correlate with much smaller MAD values between -0.12 ± 0.05 and 0.08 ± 0.05 (g kg^{-1}) h^{-1}.

From 23:30 UTC onwards, the LFD is observed to decrease rapidly to 0 (g kg^{-1}) h^{-1}, meaning that turbulence in the atmosphere is decreasing, resulting in a more stable boundary layer that is less prone to convective activity. This behaviour is also observed in Fig. 5 and Fig. 6a. Therefore, WVT is now entirely driven by MAD, e.g., the positive WVT at 24 UTC is due to advection of moist air.

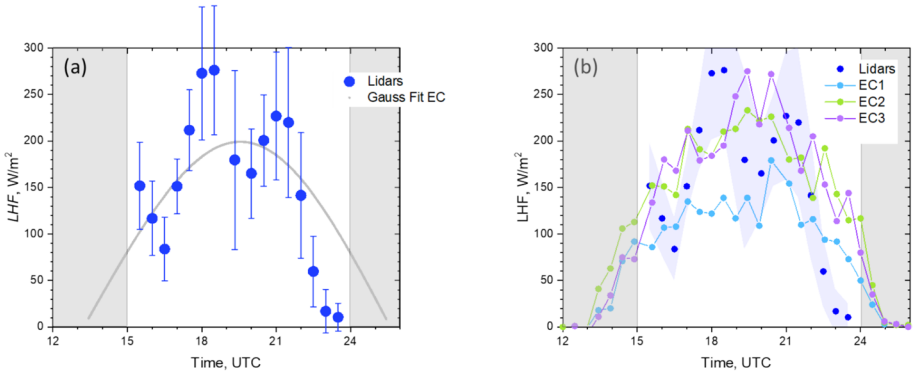

Fig. 8 LHF calculated with the combination of the vertically-ponting SRL and the vertically-ponting SDL between 0.5 z_i and 0.9 z_i. (**a**) For comparison, also the Gaussian fit of the averaged surface fluxes from the three EC towers is shown. (**b**) Compared directly with the three EC towers (Fig. 1)

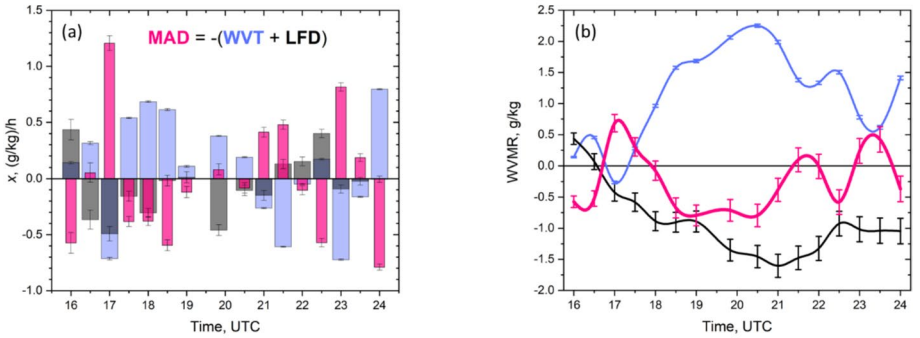

Fig. 9 (**a**) Evolution of MAD, WVT, and LFD averaged between 0.5 z_i and 0.9 z_i on August 30, between 16:00 and 24:00 UTC. The data averaged over 1 h in Fig. 6 is shown here in 30-min steps. (**b**) The three variables accumulated over the study period

Figure 9b shows the MAD, LFD and WVT accumulation over the day. The diurnal cycle can be clearly observed in the WVT and LFD plots. From midday until mid-afternoon, MAD is fairly small, because WVT is largely driven by LFD. In the morning and evening, when LHF and consequently LFD is smaller, MAD tends to be the dominant driver of WVT.

5 Summary and conclusions

In this paper, we estimate MAD from the water–vapor budget equation in the CBL. We present a methodology for doing so using a combination of vertical-pointing Raman lidar and Doppler lidar data.

We present a daytime case study at the ARM SGP site during LAFE between 15 to 24 UTC August 30, 2017, which shows a typical CBL case.

First, the high-resolution WVMR lidar data were averaged over one hour to calculate the tendency of the water–vapor mixing ratio, WVT. Second, the 10-s WVMR data were combined with one second vertical wind data measured by the DL in order to obtain the latent heat flux, LHF. For this, the data was gridded to common range and time resolutions of 50 m and 10 s. Next, the gridded data was despiked, detrendend and high-pass filtered. The resulting instantaneous turbulent fluctuations were averaged over 1 h in 10 min steps to get the mean LHF. From these LHF data covering the upper part of the CBL up to its top, we determined the LHF divergence, LFD, by calculating the vertical derivative of LHF with respect to range. Third, the moisture advection, MAD, is obtained from the sum of the negative LFD and negative WVT.

Finally, averages of LFD, WVT and MAD in the upper half of the CBL between 0.5 and 0.9 z_i are calculated. For this, z_i is determined using the maximum of the WVMR variance profile. Averaging over the upper half of the CBL reduces the random errors of WVT, and in particular, LFD to reasonable values, allowing a reliable determination of the moisture advection term MAD and thereby closure of the water–vapor budget.

This analysis was performed using only active remote sensing data, namely a synergy of a high-resolution water–vapor Raman lidar and a vertically-pointing Doppler lidar. This technique estimates the MAD locally. Comparing these results with the larger scale estimates of the approach of Wagner et al. (2022) approach, gives the same trend. Both

techniques are complementary and we foresee that both will help to further improve the understanding of the water–vapor budget in the CBL, also combined with alternative approaches (Rosenberger et al. 2024; Wakefield et al. 2023).

The water–vapor budget in the CBL is highly interesting for understanding the processes that control the moisture transport in the atmosphere and can help to better understand the sources and sinks of atmospheric moisture, the role of atmospheric dynamics in transporting moisture, and the feedbacks between moisture and cloud formation, as we observe in the case study presented in this paper. In the future, more cases with different conditions can be analysed.

This paper presents a new method for estimating the parameters of the water vapor budget equation using the combination of two pointing lidars: a water–vapor Raman lidar and a Doppler lidar.

Author contribution D.L. and A.B. wrote the main manuscript text and the figures. C.S. wrote the code used for HOM analysis. F.S. prepared the data related to the Doppler lidars. T.W. prepared the HRRR data and plot. V.W. reviewed the draft version. All authors reviewed the manuscript.

Funding Open Access funding enabled and organized by Projekt DEAL. LAFE was funded by the DOE Atmospheric System Research (ASR) program, NASA, and NOAA in the United States as well as the BMBF in Germany via the HD $(CP)^2$ project. This research was supported in part by the U.S. Department of Energy's Atmospheric System Research, an Office of Science Biological and Environmental Research program, under Grant Nos. DE-SC0014375, DE-SC0020114, and DE-SC0024048.

Data availability The Land–Atmosphere Feedback Experiment data set is freely available through the ARM Data Discovery portal (https://adc.arm.gov/discovery/).

Declarations

Ethics approval *Not applicable to this publication, since no medical or clinic data were assessed.*

Consent to participate *Not applicable.*

Consent to publish *Not applicable.*

Informed consent *The authors have given the informed consent to publish this article in the Bulletin of Atmospheric Science and Technology.*

Competing interests *Andreas Behrendt is a member of the Editorial Board of this journal, but declares he had no role in the review process of this article.*

References

Bauer HS, Späth F, Lange D, Thundathil R, Ingwersen J, Behrendt A, Wulfmeyer V (2023) Evolution of the convective boundary layer in a WRF simulation nested down to 100 m resolution

during a cloud-free case of LAFE, 2017 and comparison to observations. J Geophys Res Atmos 128(8):e2022JD037212. https://doi.org/10.1029/2022JD037212

Behrendt A, Pal S, Aoshima F, Bender M, Blyth A, Corsmeier U et al (2011) Observation of convection initiation processes with a suite of state-of-the-art research instruments during COPS IOP 8b. Q J R Meteorol Soc 137(S1):81–100. https://doi.org/10.1002/QJ.758

Behrendt A, Wulfmeyer V, Senff C, Muppa SK, Späth F, Lange D et al (2020) Observation of sensible and latent heat flux profiles with lidar. Atmos Meas Tech 13(6):3221–3233. https://doi.org/10.5194/amt-13-3221-2020

Bonin TA, Choukulkar A, Brewer WA, Sandberg SP, Weickmann AM, Pichugina YL et al (2017) Evaluation of turbulence measurement techniques from a single Doppler lidar. Atmos Meas Tech 10(8):3021–3039. https://doi.org/10.5194/AMT-10-3021-2017

Choukulkar A, Brewer WA, Sandberg SP, Weickmann A, Bonin TA, Hardesty RM et al (2017) Evaluation of single and multiple Doppler lidar techniques to measure complex flow during the XPIA field campaign. Atmos Meas Tech 10(1):247–264. https://doi.org/10.5194/amt-10-247-2017

Di Girolamo P, Cacciani M, Summa D, Scoccione A, De Rosa B, Behrendt A, Wulfmeyer V (2017) Characterisation of boundary layer turbulent processes by the Raman lidar BASIL in the frame of HD(CP)^2 observational prototype experiment. Atmos Chem Phys 17(1):745–767. https://doi.org/10.5194/ACP-17-745-2017

Goldsmith JEM, Blair FH, Bisson SE, Turner DD (1998) Turn-key raman lidar for profiling atmospheric water vapor, clouds, and aerosols. Appl Opt 37(21):4979. https://doi.org/10.1364/ao.37.004979

Hammann E, Behrendt A, Le Mounier F, Wulfmeyer V (2015) Temperature profiling of the atmospheric boundary layer with rotational Raman lidar during the HD(CP)2 observational prototype experiment. Atmos Chem Phys 15(5):2867–2881. https://doi.org/10.5194/acp-15-2867-2015

Lange D, Behrendt A, Muppa SK, Wulfmeyer V, Lange D, Behrendt A, et al (2019) Compact automatic rotational Raman lidar system for continuous day- and nighttime temperature and humidity mapping. *EGUGA*, 7010. https://doi.org/10.1029/2019GL085774

Lenschow DH, Mann J, Kristensen L (1994) How long is long enough when measuring fluxes and other turbulent statistics? J Atmos Ocean Technol 11(3):661–673. https://doi.org/10.1175/1520-0426(1994)011%3c0661:HLILEW%3e2.0.CO;2

Lenschow DH, Wulfmeyer V, Senff C, Lenschow DH, Wulfmeyer V, Senff C (2000) Measuring second- through fourth-order moments in noisy data. J Atmos Oceanic Tech 17(10):1330–1347. https://doi.org/10.1175/1520-0426(2000)017%3c1330:MSTFOM%3e2.0.CO;2

Lenschow DH, Lothon M, Mayor SD, Sullivan PP, Canut G (2012) A comparison of higher-order vertical velocity moments in the convective boundary layer from lidar with in situ measurements and large-eddy simulation. Boundary-Layer Meteorol 143(1):107–123. https://doi.org/10.1007/S10546-011-9615-3

Michael P (1994) Estimating advective tendencies from field measurements. Mon Weather Rev 122(9):2202–2209. https://doi.org/10.1175/1520-0493(1994)122%3c2202:EATFFM%3e2.0.CO;2

Muppa SK, Behrendt A, Späth F, Wulfmeyer V, Metzendorf S, Riede A (2016) Turbulent humidity fluctuations in the convective boundary layer: case studies using water vapour differential absorption lidar measurements. Boundary-Layer Meteorol 158(1):43–66. https://doi.org/10.1007/S10546-015-0078-9

Pearson G, Davies F, Collier C (2009) An analysis of the performance of the UFAM pulsed Doppler lidar for observing the boundary layer. J Atmos Ocean Technol 26(2):240–250. https://doi.org/10.1175/2008JTECHA1128.1

Radlach M, Behrendt A, Wulfmeyer V (2008) Scanning rotational Raman lidar at 355 nm for the measurement of tropospheric temperature fields. Atmos Chem Phys 8(2):159–169. https://doi.org/10.5194/acp-8-159-2008

Rosenberger TE, Heus T, Raghunathan GN, Turner DD, Wagner TJ, Simonson JM (2024) An LES exploration of the assumptions used in retrieving entrainment from a mixing diagram approach with ground-based remote sensors. https://doi.org/10.5194/EGUSPHERE-2024-2894

Santanello JA Jr, Peters-Lidard CD, Kumar SV (2011) Diagnosing the sensitivity of local land-atmosphere coupling via the soil moisture-boundary layer interaction. Journal of Hydrometeorology 12(5):766–786. https://doi.org/10.1175/JHM-D-10-05014.1

Senff C, Bösenberg J, Peters G (1994) Measurement of water vapor flux profiles in the convective boundary layer with lidar and Radar-RASS. J Atmos Ocean Technol 11. American Meteorological Society. https://doi.org/10.1175/1520-0426(1994)011<0085:MOWVFP>2.0.CO;2

Sisterson DL, Peppler RA, Cress TS, Lamb PJ, Turner DD (2016) The ARM Southern Great Plains (SGP) Site. Meteorol Monogr 57(1):6.1-6.14. https://doi.org/10.1175/AMSMONOGRAPHS-D-16-0004.1

Späth F, Behrendt A, Kumar Muppa S, Metzendorf S, Riede A, Wulfmeyer V (2016) 3-D water vapor field in the atmospheric boundary layer observed with scanning differential absorption lidar. Atmos Meas Tech 9(4):1701–1720. https://doi.org/10.5194/AMT-9-1701-2016

Späth F, Behrendt A, Brewer WA, Lange D, Senff C, Turner DD et al (2022) Simultaneous observations of surface layer profiles of humidity, temperature, and wind using scanning lidar instruments. J Geophys Res Atmos 127(5):e2021JD035697. https://doi.org/10.1029/2021JD035697

Thorsen TJ, Fu Q (2015) Automated retrieval of cloud and aerosol properties from the ARM Raman lidar. Part II: Extinction. J Atmos Ocean Technol 32(11):1999–2023. https://doi.org/10.1175/JTECH-D-14-00178.1

Turner DD, Blumberg WG (2019) Improvements to the AERIoe thermodynamic profile retrieval algorithm. IEEE J Sel Top Appl Earth Obs Remote Sens 12(5):1339–1354. https://doi.org/10.1109/JSTARS.2018.2874968

Turner DD, Goldsmith JE (1999) Twenty-four-hour Raman lidar water vapor measurements during the Atmospheric Radiation Measurement Program's 1996 and 1997 water vapor intensive observations periods. J Atmos Ocean Technol 16:1062–1076. https://doi.org/10.1175/1520-0426(1999)016%3c1062:tfhrlw%3e2.0.co

Turner DD, LöHnert U (2014) Information content and uncertainties in thermodynamic profiles and liquid cloud properties retrieved from the ground-based atmospheric emitted radiance interferometer (AERI). J Appl Meteorol Climatol 53(3):752–771. https://doi.org/10.1175/JAMC-D-13-0126.1

Turner DD, Lohnert U (2021) Ground-based temperature and humidity profiling: combining active and passive remote sensors. Atmos Meas Tech 14(4):3033–3048. https://doi.org/10.5194/AMT-14-3033-2021

Turner DD, Ferrare RA, Brasseur LAH, Feltz WF, Tooman TP (2002) Automated retrievals of water vapor and aerosol profiles from an operational Raman lidar. J Atmos Oceanic Tech 19(1):37–50. https://doi.org/10.1175/1520-0426(2002)019%3c0037:AROWVA%3e2.0.CO;2

Turner DD, Wulfmeyer V, Berg LK, Schween JH (2014) Water vapor turbulence profiles in stationary continental convective mixed layers. J Geophys Res Atmos 119(19):11151–11165. https://doi.org/10.1002/2014JD022202

Wagner G, Behrendt A, Wulfmeyer V, Späth F, Schiller M (2013) High-power Ti:sapphire laser at 820 nm for scanning ground-based water–vapor differential absorption lidar. Appl Opt 52(11):2454–2469. https://doi.org/10.1364/AO.52.002454

Wagner TJ, Turner DD, Heus T, Blumberg WG (2022) Observing profiles of derived kinematic field quantities using a network of profiling sites. J Atmos Ocean Technol 39(3):335–351. https://doi.org/10.1175/JTECH-D-21-0061.1

Wakefield RA, Turner DD, Rosenberger T, Heus T, Wagner TJ, Santanello J, Basara J (2023) A methodology for estimating the energy and moisture budget of the convective boundary layer using continuous ground-based infrared spectrometer observations. J Appl Meteorol Climatol 62(7):901–914. https://doi.org/10.1175/JAMC-D-22-0163.1

Weckwerth TM, Wulfmeyer V, Wakimoto RM, Hardesty RM, Wilson JW, Banta RM (1999) NCAR-NOAA lower tropospheric water-vapor workshop. Bull Am Meteorol Soc 80:2339–2357. https://doi.org/10.1175/1520-0477(1999)080%3c2339:nnltwv%3e2.0.co

Whiteman DN (2003a) I. Evaluating the temperature-dependent lidar equations. Appl Optics 42(15):2571–2592. https://doi.org/10.1364/AO.42.002571

Whiteman DN (2003b) II. Evaluating the ratios for water vapor and aerosols. Appl Optics 42(15):2593–2608. https://doi.org/10.1364/AO.42.002593

Wulfmeyer V, Pal S, Turner DD, Wagner E (2010) Can water vapour raman lidar resolve profiles of turbulent variables in the convective boundary layer? Boundary-Layer Meteorol 136(2):253–284. https://doi.org/10.1007/S10546-010-9494-Z

Wulfmeyer V, Hardesty RM, Turner DD, Behrendt A, Cadeddu MP, Di Girolamo P et al (2015) A review of the remote sensing of lower tropospheric thermodynamic profiles and its indispensable role for the understanding and the simulation of water and energy cycles. Rev Geophys 53(3):819–895. https://doi.org/10.1002/2014RG000476

Wulfmeyer V, Muppa SK, Behrendt A, Hammann E, Späth F, Sorbjan Z et al (2016) Determination of convective boundary layer entrainment fluxes, dissipation rates, and the molecular destruction of variances: theoretical description and a strategy for its confirmation with a novel lidar system synergy. J Atmos Sci 73(2):667–692. https://doi.org/10.1175/JAS-D-14-0392.1

Wulfmeyer V, Turner DD, Baker B, Banta R, Behrendt A, Bonin T et al (2018) A new research approach for observing and characterizing land-atmosphere feedback. Bull Am Meteorol Soc 99(8):1639–1667. https://doi.org/10.1175/BAMS-D-17-0009.1

Wulfmeyer V (1999) Investigation of Turbulent Processes in the Lower Troposphere with Water Vapor DIAL and Radar-RASS. J Atmos Sci 56. American Meteorological Society. https://doi.org/10.1175/1520-0469(1999)056<1055:IOTPIT>2.0.CO;2